Toward unbiased flow measurements in *pp* collisions at the CERN Large Hadron Collider

S. Ji,[1,*] M. Virta,[2,3] T. Kallio,[2] S. H. Lim,[1] and D. J. Kim[2,3]

[1]*Pusan National University, Department of Physics, Busan 46241, Republic of Korea*
[2]*University of Jyväskylä, Department of Physics, P.O. Box 35, FI-40014 University of Jyväskylä, Finland*
[3]*Helsinki Institute of Physics, P.O.Box 64, FI-00014 University of Helsinki, Finland*

(Received 18 March 2023; revised 20 July 2023; accepted 18 August 2023; published 18 September 2023)

Long-range correlations for pairs of charged particles with two-particle angular correlations are studied in *pp* at $\sqrt{s} = 13$ TeV with various Monte Carlo generators. The correlation functions are constructed as functions of the relative azimuthal angle $\Delta\varphi$ and the pseudorapidity separation $\Delta\eta$ for pairs of different particle species with the identified hadrons such as π, K, p, and Λ in wide $\Delta\eta$ ranges. Fourier coefficients are extracted for the long-range correlations in several-multiplicity classes using a low-multiplicity template fit method. The method allows one to subtract the enhanced away-side jet fragments in high-multiplicity events with respect to low-multiplicity events. However, we found that due to a kinematic bias on jets and differing model implementation of flow and jet components, subtracting the nonflow contamination in small systems can bias the results. It is found that the PYTHIA8 default model where the presence of the collective flow is not expected but the bias results in very large flow. Also extracting flow signal from the EPOS4 and PYTHIA8 string shoving models is not possible because of the flow signal introduced in the low-multiplicity events. Only a multiphase transport string melting model among studied model calculations is free from this bias and shows a mass ordering at low p_{T} and particle type grouping in the intermediate-p_{T} range. This feature was first observed in large systems, but the mass ordering in small systems differs from that observed in large collision systems.

DOI: 10.1103/PhysRevC.108.034909

I. INTRODUCTION

Collisions between heavy ions (HICs) exhibit strong collectivity, as demonstrated by the anisotropy in the momentum distribution of final particles emitted at the BNL Relativistic Heavy Ion Collider (RHIC) [1–4] and the CERN Large Hadron Collider (LHC) [5–7]. The spatial anisotropies are converted to anisotropies in the final momentum distribution due to a pressure-driven expansion of the strongly interacting quark-gluon plasma (QGP) formed during the collision event. The produced QGP in HICs is in the strongly coupled regime and the state-of-the-art Bayesian analyses utilizing the experimental data favor small values of the shear viscosity to entropy density ratio (η/s), which implies that the produced QGP is considered to be the fluid with the lowest shear viscosity to entropy density ratio observed in nature [8,9]. In recent years, the primary focus has been to constrain model parameters by measuring sensitive observables, using Bayesian analyses [10–15].

To probe the collective behavior in the momentum anisotropy, long-range particle correlations are used over a wide range of pseudorapidity. Over the past few years, long-range correlations have also been observed in smaller collision systems, such as high-multiplicity (HM) proton-proton (pp) collisions [16–20], proton-nucleus (pA) collisions [21–24], and collisions of light ions with heavy ions, such as p + Au, d + Au, and ^{3}He +Au [25,26]. These observations raise the question of whether small system collisions have an underlying mechanism for developing correlations similar to that of heavy AA collisions.

On the experimental side, extracting flow in small systems remains challenging due to a strong jet fragmentation bias to the long-range correlations. One commonly used approach for suppressing the nonflow contribution in two-particle correlations is to require a large $\Delta\eta$ gap between the two particles, which is also applied in cumulant methods [19,27]. However, this approach only eliminates nonflow contributions on the near side, not on the away side ($\Delta\varphi \sim \pi$). To address this limitation, a low-multiplicity template fit (LMTF) method has been proposed to remove away-side contributions as well [16,23,28], taking into account the autocorrelation between event multiplicity and jet yields [29]. This method enables the subtraction of enhanced away-side jet yields in HM events compared to low-multiplicity (LM) events, and it may potentially provide a lower limit on the event multiplicity needed to observe the flow signal.

The observed scaling pattern of the elliptic flow with respect to the number of constituent quarks (NCQ) in large collision systems at RHIC [30–33] and LHC [6,34–37] suggests the creation of a thermalized bulk system of quarks that coalesce into hadrons. However, it is known that NCQ scaling

*su-jeong.ji@cern.ch

is an approximate argument and is not expected to be exact. For example, Ref. [38] demonstrates that NCQ scaling is impacted by the initial conditions for the evolution of the parton phase as well as by interactions in the hadronic phase. Another study [39] shows the violation of NCQ scaling due to finite baryon density and high phase-space density of partons [40]. Although the scaling in large collision systems is observed to hold at an approximate level of 20% [36,37], the question of whether these patterns can still be observed in collisions of small systems is of great current interest. Understanding how the NCQ scaling in smaller systems is different from that in large systems would provide important insights into the underlying physics of the system. An approximate NCQ scaling of charged hadrons' v_2 in p-Pb collisions at $\sqrt{s_{\rm NN}} = 5.02$ TeV is observed at intermediate $p_{\rm T}$ by the ALICE Collaboration [41] and also for v_2 of π and p in ^{3}He +Au collisions at $\sqrt{s_{\rm NN}}$ = 200 GeV by the PHENIX Collaboration [42]. However, this observation was based on a limited range of $p_{\rm T}$ with the cumulant methods and further experimental checks are needed to confirm the presence of NCQ scaling over a wider range of $p_{\rm T}$ with the experimental LMTF method. Additionally, it is important to note that other effects, such as initial-state fluctuations and final-state correlations, can also contribute to the observed elliptic flow in small systems. Therefore, more detailed studies are needed to understand the interplay of these effects and the possible mechanisms underlying the observed NCQ scaling patterns.

On the theoretical side, systematic mapping of the multiparticle correlations across collision systems by varying sizes is presently under way (see, e.g., Ref. [43]). The quantitative description of the full set of experimental data has not been achieved yet. A summary of various explanations for the observed correlations in small systems is given in Refs. [44–46].

Another important piece of evidence for a strongly interacting medium in small collision systems would be the presence of jet quenching [47,48]. However, no evidence of jet quenching has been observed in either HM pp or p-Pb collisions [49–53]. A study with two-particle angular correlations in short-range correlations around $(\Delta\eta, \Delta\varphi) = (0, 0)$ is a good tool for studying jet fragmentations [54].

This report investigates the relationship between jet production and collective phenomena in small systems using various Monte Carlo event generators, such as a multiphase transport (AMPT) string melting model [55], PYTHIA8 string shoving [56,57], and EPOS4 [58]. Although all three models incorporate both jets and collective flow effects, they differ in their approach to describing collective flow. To determine the suitability of each model for a specific experimental method, we assess the latest flow extraction technique, LMTF, against these models. This paper is organized as follows. First, the model descriptions are given in Sec. II and analysis methods are described in Sec. III. The results from model calculations are presented in Sec. IV. Finally, the results are summarized in Sec. V.

II. MODEL DESCRIPTIONS

In this study, several Monte Carlo (MC) event generators, such as PYTHIA8, AMPT, and EPOS4, of different characteristics are used to compare the nonflow subtraction results. We generate a few million pp collision events with each event generator and collect final-state charged particles for further analysis. Here we have a brief description of the event generators.

PYTHIA8. PYTHIA8 is a widely used event generator for high-energy pp collisions, and it has recently incorporated a capability of heavy-ion collisions. It includes both hard and soft interactions for jets and underlying events, and the default parameter set called the Monash tune can reasonably describe the production of soft particles [59]. In the default version, there is no partonic or hadronic interaction, so we do not expect a long-range correlation among produced particles due to the flow contribution. Hence, it has been used to verify methods to estimate the nonflow contribution [60].

PYTHIA8 string shoving. In PYTHIA8, a model to describe the long-range correlation in HM pp collisions called "string shoving" has been implemented as an option [56,57]. This model introduces a repulsive force between strings, and the interaction can cause a microscopic transverse pressure, giving rise to the long-range correlations. The string shoving approach in PYTHIA8 successively reproduces the experimental measurements of the long-range near-side ($\Delta\varphi \sim 0$) ridge yield in HM pp events by the ALICE Collaboration [61] and the CMS Collaboration [18]. However, strings produced from hard scatterings are also affected by the repulsive force, which then leads to observed long-range correlation even in low-multiplicity events [62].

AMPT. Besides several models based on the causal hydrodynamic framework in describing the collective evolution in small collision systems, the AMPT model with string melting [55] can reproduce the flowlike signals by modeling the evolution of medium as a collection of interacting quarks and hadrons [63]. The applicability of fluid-dynamical simulations and partonic cascade models in small systems has been explored in Ref. [64]. In the context of kinetic theory with isotropization-time approximation, the model can smoothly explain the long-range correlations by fluidlike (hydrodynamic) excitations for Pb-Pb collisions and particlelike (or nonhydrodynamic) excitations for pp or p-Pb collisions [65–67]. This study uses the parton cross section value of 3 mb, which is the same as the one used in larger system studies [55]. The value of the parton cross sections is crucial as they affect the final-state observables.

EPOS4 . The EPOS model describes the full evolution of medium produced by heavy-ion collisions with two parts called a core and a corona [68]. The core part follows the hydrodynamic expansion, and the corona part is composed of hadrons from string decays. After the hadronization process of the core part, the ultrarelativistic quantum molecular dynamics model is used to describe hadronic interactions among all hadrons from two parts. The version called EPOS LHC including a different type of radial flow in the case of a small but a very dense system can successfully describe the long-range correlation in HM pp events [61]. Recently, a new version of EPOS (*EPOS4*) has been released to the public. We utilize the framework for this study.

The summary of the model characteristics is listed in Table I. The PYTHIA8 default model is used to understand the nonflow contributions. The PYTHIA8 shoving, AMPT, and

TABLE I. A list of the models used in this paper.

Models	Characteristics	Mechanism
PYTHIA8 default	Jets and no flow	Ref. [59]
PYTHIA8 shoving	Jets and flow	String repulsion [56,57]
AMPT	Jets and flow	String melting [55]
EPOS4	Jets and hydro	Core (hydrodynamical) [58]

EPOS4 models all include both jets and collective flow effects. However, they differ in their mechanisms for describing the collective flow. It is important to note that the applicability of each model to a specific experimental method may depend on various factors, such as the collision system being studied, as well as the specific observables being measured. Therefore, it is important to carefully consider the strengths and limitations of each model when interpreting experimental results. For instance, in the study by the ALICE Collaboration [61], both PYTHIA8 shoving and EPOS4 fail to reproduce the near-side jet yields, with PYTHIA8 shoving predicting an increasing near-side jet yield with increasing multiplicity, while EPOS4 shows the opposite trend. Regarding the ridge yields, EPOS4 overestimates them, while PYTHIA8 shoving underestimates them. The ridge yields in low-multiplicity events are similar to those in HM events for EPOS4 and PYTHIA8 shoving, while they decrease towards low multiplicity events in the experimental data [17].

III. ANALYSIS PROCEDURE

A. Event and particle selections

This analysis uses the same event selection criteria as the ALICE experiments, which require a charged particle in both V0A and V0C [70,71] acceptance. V0A and V0C cover the pseudorapidity ranges $2.8 < \eta < 5.1$ and $-3.7 < \eta < -1.7$, respectively. The contribution from diffractive interactions is minimized in these events [69]. Figure 1 shows the charged-particle density in various p_{T} intervals. Every model describes the trend of the data well, while PYTHIA8 string shoving and AMPT models overestimate the data from the ALICE Collaboration [69]. Despite the PYTHIA8 string shoving model largely overestimating the data, the p_{T} dependency is similar to that of the PYTHIA8 default and EPOS4 models. In the case of the AMPT model, it shows a different p_{T} dependency.

The multiplicity percentiles are estimated by V0M, which is the sum of the charged particles in both the V0A and the V0C acceptance. The event multiplicity of V0M from different generators is shown in Fig. 2. The PYTHIA8 string shoving model generates HM events more than other models. The vertical lines indicates the 0–5%, 5–20%, and 60–100% event multiplicity of the AMPT string melting events. For the identified flow measurement, π, K, and p for all models and additionally Λ for the AMPT model are studied by selecting the particle identification code from the models in the range of $0.2 < p_{\mathrm{T}} < 6$ GeV/c.

B. Two-particle angular correlations

Two-particle angular correlations are measured as functions of the relative azimuthal angle ($\Delta\varphi$) and the relative pseudorapidity ($\Delta\eta$) between a trigger and associated

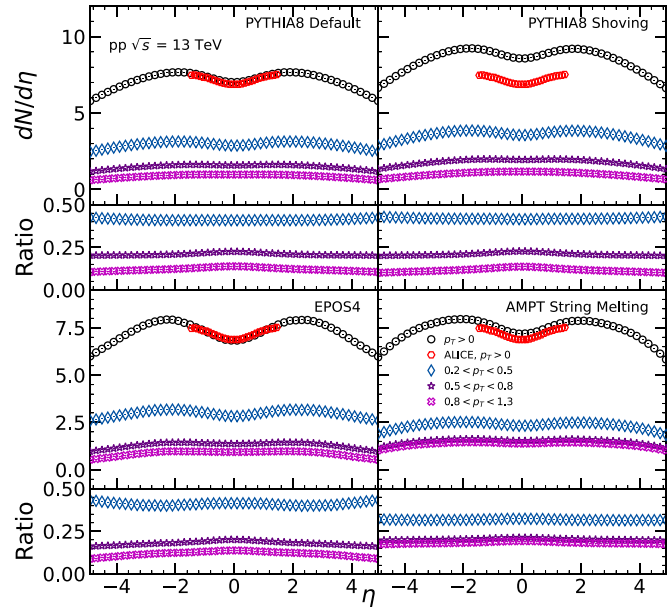

FIG. 1. Charged-particle pseudorapidity density for four different p_{T} intervals over broad η ranges in several model calculations is compared to the ALICE data [69].

particles:

$$\frac{1}{N_{\mathrm{trig}}}\frac{d^2N_{\mathrm{pair}}}{d\Delta\eta d\Delta\varphi} = B_{\mathrm{max}}\frac{S(\Delta\eta,\Delta\varphi)}{B(\Delta\eta,\Delta\varphi)}\bigg|_{p_{\mathrm{T,trig}},\,p_{\mathrm{T,assoc}}}, \qquad (1)$$

where the trigger and the associated particles are defined for different transverse momentum ranges and different η acceptance of the detectors. N_{trig} and N_{pair} are the numbers of trigger particles and trigger-associated particle pairs, respectively. $S(\Delta\eta,\Delta\varphi)$ corresponds to the average number of pairs in the same event and $B(\Delta\eta,\Delta\varphi)$ to the number of pairs in mixed events. B_{max} represents the normalization of $B(\Delta\eta,\Delta\varphi)$, and by dividing $S(\Delta\eta,\Delta\varphi)$ with $B(\Delta\eta,\Delta\varphi)/B_{\mathrm{max}}$ the acceptance effects are corrected for. This analysis is performed for several multiplicity percentiles (0–5%, 0–20%, 20–40%, and 60–100%) and for each multiplicity percentile.

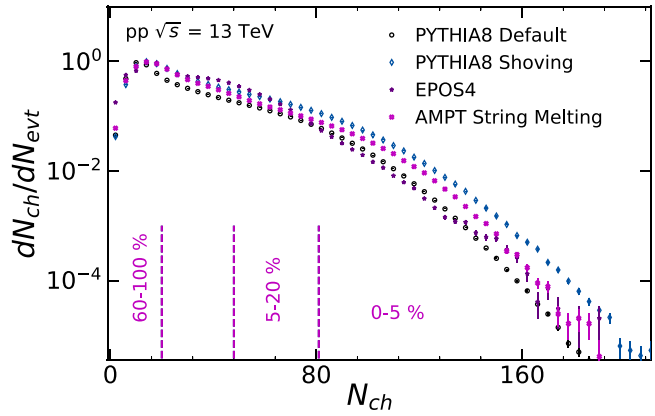

FIG. 2. The distribution of the V0M charged particles in the regions $-3.7 < \eta < -1.7$ and $2.8 < \eta < 5.1$. This is used to determine the event multiplicity classes in *pp* collisions at $\sqrt{s} = 13$ TeV.

TABLE II. The acceptance of the detectors used for the trigger and/or associated particles.

Detector	η acceptance	p_T range
TPC	$\lvert\eta\rvert < 0.8$	$0.2 < p_T < 6.0$ GeV/c
FMDA	$1.9 < \eta < 4.8$	$p_T > 0.0$ GeV/c
FMDC	$-3.1 < \eta < -1.9$	$p_T > 0.0$ GeV/c

TABLE III. The $\lvert\Delta\eta\rvert$ ranges of each correlation function and four additional wider $\Delta\eta$ gaps used to further reduce the nonflow contributions.

Correlations	Default	Gap-A	Gap-B	Gap-C	Gap-D
TPC-FMDA	[1.1, 5.6]	[1.5, 5.6]	[2.0, 5.6]	[2.5, 5.6]	[3.0, 5.6]
TPC-FMDC	[1.1, 3.9]	[1.6, 3.9]	[2.0, 3.9]	[2.5, 3.9]	[3.0, 3.9]
FMDA-FMDC	[3.8, 7.9]	[4.3, 7.9]	[4.8, 7.9]	[5.3, 7.9]	[5.8, 7.9]

The flow studies using the ALICE detector were carried out using only the particles detected in the time projection chamber (TPC) detector [69]. However, due to the limited η acceptance of the TPC detector, the study was restricted to the edge of the detector with $1.6 < \Delta\eta| < 1.8$, as well as $p_T > 1.0$ GeV/c to avoid nonflow contributions [69]. To further suppress nonflow contributions, preliminary studies by the ALICE experiment have used the very forward forward multiplicity detector (FMD) detectors to achieve a large η separation of the correlated particles, up to $|\Delta\eta| \approx 6$. In this analysis, we use the same combinations of correlations between particles in the TPC and FMD detectors.

Table II lists the η acceptance and the measurable p_T ranges for each detector used in the analysis.

As for TPC-FMD correlations, the trigger particles are from TPC detectors with various p_T intervals and the associated particles are from forward multiplicity detector A (FMDA) and forward multiplicity detector C (FMDC) in different η ranges with $p_T > 0.0$ GeV/c. As for FMDA-FMDC correlations, both trigger and associated particles come from the FMD detector with $p_T > 0.0$ GeV/c. The $\Delta\eta$ ranges used for the default analysis with the full η acceptance of all detectors and four additional wider $\Delta\eta$ gaps used to further reduce the nonflow contributions are summarized in Table III.

Figures 3 and 4 show the two-dimensional correlation function of each detector combination with the events from PYTHIA8 default and AMPT string melting models, respectively. Unlike the events from AMPT having both flow and jet components, the PYTHIA8 default events contain the particles purely from jets. The peak seen in the short range represents the jet contribution. Even though we already have long-range correlations by using the particles in the TPC and FMD detectors, still the large jet contamination is seen. To find a safe long-range region for the analysis, five different long ranges are selected to study the effect on the degree of the jet contamination. Different shapes and amplitudes of the jet peak are seen depending on the models.

In the next section, the details about the LMTF method, which is used for the nonflow subtraction, are discussed as well as the assumptions of the method.

C. Extraction of flow coefficients from the low-multiplicity template fit method

Due to the strong jet fragmentation bias in small collision systems it is difficult to extract the flow in these collisions

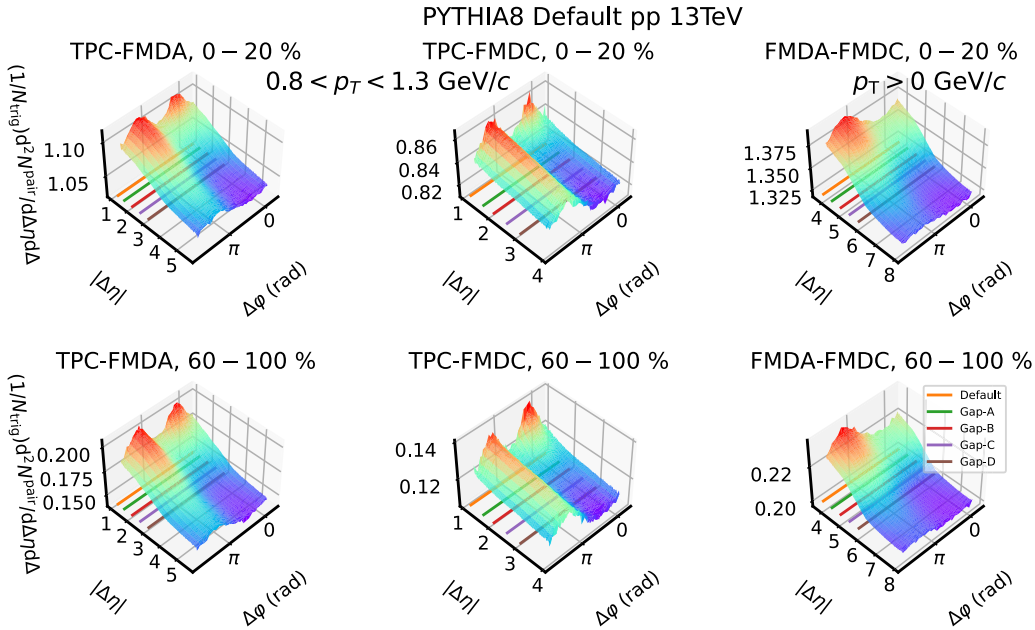

FIG. 3. Two-particle correlation functions as functions of $\Delta\eta$ and $\Delta\varphi$ for HM (0–20%, top panels) and LM (60–100%, bottom panels) events using different combinations of the detectors in $\sqrt{s} = 13$ TeV pp collisions from AMPT string melting calculations. The intervals of $p_{T,\,\mathrm{trig}}$ and $p_{T,\,\mathrm{assoc}}$ are $0.8 < p_T < 1.3$ GeV/c with TPC and $p_T > 0$ GeV/c with FMDA or FMDC.

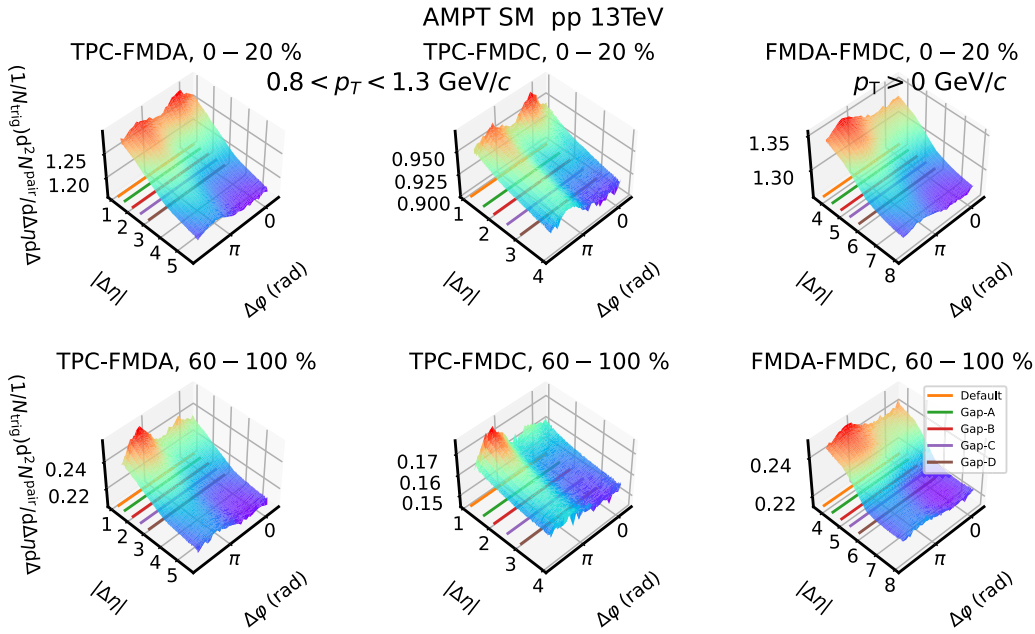

FIG. 4. Two-particle correlation functions as functions of $\Delta\eta$ and $\Delta\varphi$ for HM (0–20%, top panels) and LM (60–100%, bottom panels) events using different combinations of the detectors in $\sqrt{s} = 13$ TeV pp collisions from PYTHIA8 default calculations. The intervals of $p_{\mathrm{T,\,trig}}$ and $p_{\mathrm{T,\,assoc}}$ are $0.8 < p_{\mathrm{T}} < 1.3$ GeV/c with TPC and $p_{\mathrm{T}} > 0$ GeV/c with FMDA or FMDC.

because of the remaining nonflow in the away-side region ($\Delta\varphi \sim \pi$) in Eq. (1). As discussed in Refs. [16,23], the HM correlation function in a HM percentile can be expressed as

$$Y_{\mathrm{HM}}(\Delta\varphi) = G[1 + 2v_{2,2}\cos(2\Delta\varphi) + 2v_{3,3}\cos(3\Delta\varphi) + 2v_{4,4}\cos(4\Delta\varphi)] + F\,Y_{\mathrm{LM}}(\Delta\varphi), \quad (2)$$

where $Y_{\mathrm{LM}}(\Delta\varphi)$ is the LM correlation function, G is the normalization factor for the Fourier component up to the fourth harmonic, and the scale factor F corresponds to the relative away-side jetlike contribution with respect to the LM (the 60–100%). This method assumes that Y_{LM} does not contain a peak in the near side originating from jet fragmentation and that the jet shape remains unchanged in HM events compared to LM events. The first assumption is well verified using the selected LMTF method for the experimental data [28], while the second assumption regarding the modification of jet shapes is tested using the near-side $\Delta\eta$ distributions. Additionally, the ATLAS Collaboration's study of HM pp and p-Pb collisions in Ref. [28] provides further support for this assumption, as there is no evidence of jet quenching in these collisions [49–53]. The fit determines the scale factor F and the pedestal G, and $v_{n,n}$ are calculated from a Fourier transform. It is worthwhile noting that this method does not rely on the zero yield at minimum hypothesis to subtract an assumed flat combinatorial component from the LMTF as done previously in Refs. [22,72]. Whether or not the models agree on the assumption about the jet shape modification depending on the event multiplicity is discussed in Sec. IV.

Figure 5 shows the LMTF results of the TPC-FMDA correlation for the 0–20% multiplicity percentile from the AMPT string melting configuration. Even with the PYTHIA8 default $\Delta\eta$ gap, no ridge structure on the near side is seen in LM correlation function, which indicates that there is almost no jet contamination. The figure also shows the $v_{2,2}$ and $v_{3,3}$ components, yet the $v_{2,2}$ component is dominant.

The low-multiplicity templates of each $\Delta\eta$ gap are seen in Fig. 6. As the jet shape is well described in PYTHIA8 default, the comparison is done using the PYTHIA8 model. Each template is normalized by its $\Delta\eta$. A decreasing near-side yield is seen with a increasing $\Delta\eta$ gap (from the default gap to gap-D), and almost the same feature is seen in gap-C and gap-D.

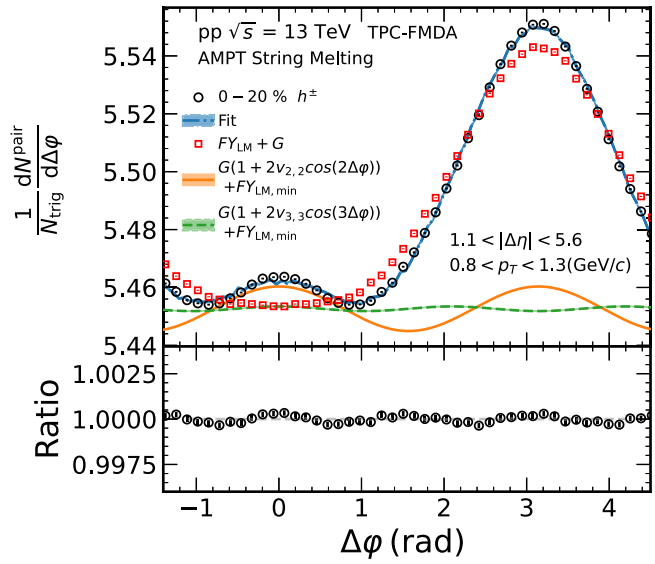

FIG. 5. The low-multiplicity template fit results. The black markers shows the signal for the 0–20% multiplicity percentile together with its fit shown as a blue band. The red squares correspond to the low-multiplicity template. The orange and green curves correspond to the extracted v_2 and v_3 signals, respectively.

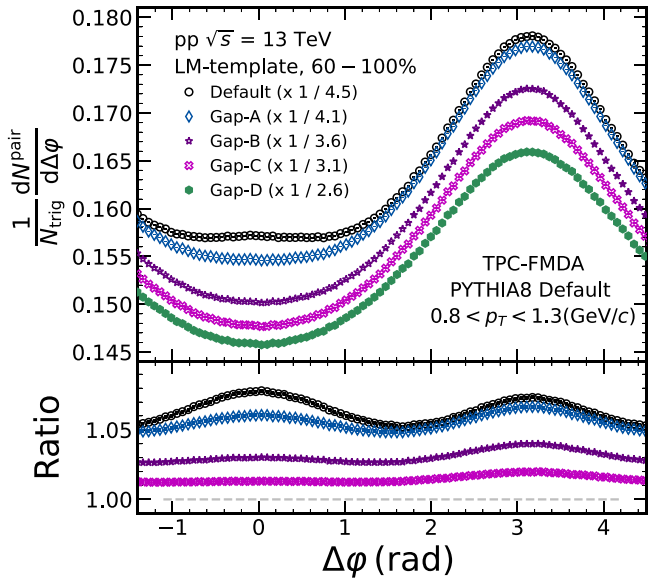

FIG. 6. The $\Delta\eta$-gap-dependent low-multiplicity templates with PYTHIA8 default.

Under the first assumption of the template fit method, which requires no near-side yield in the low-multiplicity events, we selected the gap-D for the precise analysis. To see if the other models meet the assumption, the low-multiplicity templates of each model are compared in gap-D.

The comparison between the low-multiplicity templates of each model in the default $\Delta\eta$ gap is seen in the Fig. 7. As the near-side yield in the LM events comes from the jets, there should be no near-side ridge yield for the precise nonflow subtraction. The presence of the LM jet bias indicates that there is a chance of the jet shape modification in the away side. The ratio is calculated by dividing the AMPT string melting

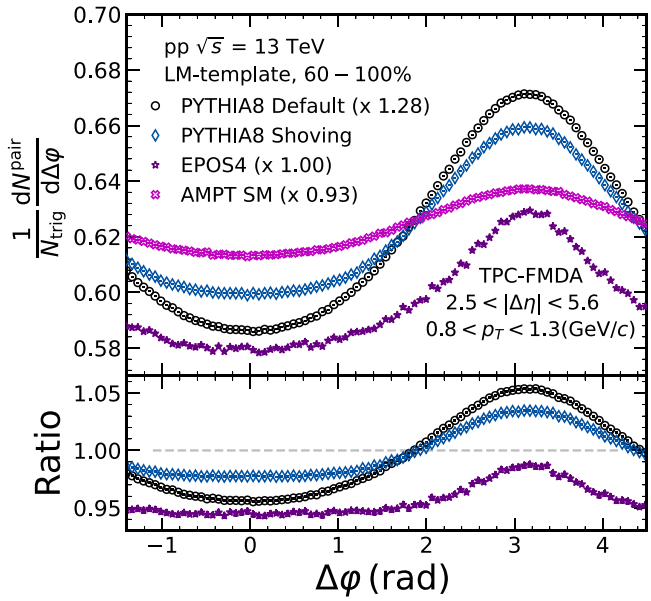

FIG. 7. The LM template for the different model calculations using the default gap.

from the PYTHIA8 default, PYTHIA8 string shoving, and EPOS4 models. The PYTHIA8 model shows a small near-side yield and the string shoving model shows a larger yield, whilst there is no ridge yield from the AMPT string melting and the EPOS4 models. In the case of the away-side yield, a fairly broad shape is seen in the AMPT string melting version and a narrow shape is seen in the EPOS4 version compared to both PYTHIA8 configurations.

However, we cannot test whether the models agree with the second assumption requiring no jet shape modification depending on the event multiplicity. As every model apart from the PYTHIA8 default contains the flow components in the away side, we can not disentangle the flow and jets.

Finally, v_n values are extracted, based on the observed factorization of $v_{n,n}$ to single harmonics [16,23], using the following equation,

$$v_n(p_{\mathrm{T,TPC}}) = \sqrt{\frac{v_{n,n}^{\mathrm{TPC-FMDA}} v_{n,n}^{\mathrm{TPC-FMDC}}}{v_{n,n}^{\mathrm{FMDA-FMDC}}}}, \tag{3}$$

where $v_{n,n}(p_{\mathrm{T,trig}}$ and $p_{\mathrm{T,assoc}})$ are measured in $0.2 < p_{\mathrm{T,trig}} < 6$ GeV/c and integrated p_{T} ranges.

IV. RESULTS

A. Unidentified charged hadron flow

The p_{T}-differentials v_2 of the charged particles for different $\Delta\eta$ gap intervals in pp collisions at $\sqrt{s} = 13$ TeV are shown in Fig. 8 for several model calculations. The top panels show the final v_2 and the bottom two rows of panels show $v_{2,2}$ measured from TPC-FMDA and TPC-FMDC, respectively. The results for PYTHIA8 default are shown in the first column, those for PYTHIA8 string shoving are shown in the second column, those for EPOS4 are shown in the third co[umn, and those for AMPT string melting are shown in the last column. Even though the PYTHIA8 default medel does not contain any flow component, nonzero v_2 is seen in every $\Delta\eta$ gap. As the $\Delta\eta$ gap becomes larger, the less nonflow dominant region we contain as shown in the Fig. 3; therefore, a smaller amplitude of v_2 is seen with an increasing $\Delta\eta$ gap. Despite the PYTHIA8 string shoving model having both flow and nonflow components, similar behavior is observed with the PYTHIA8 default model, albeit with a smaller magnitude of the flow component overall. This can be due to the presence of the near-side yield in the low multiplicity which can be seen in the LMTF results. In the case of the EPOS4 model, which also includes the flow components, smaller magnitudes of v_2 and $v_{2,2}$ are seen compared to both PYTHIA8 configurations and similar p_{T} and $\Delta\eta$ gap dependencies are seen with PYTHIA8. Lastly, the AMPT string melting model shows that in low-p_{T} regions v_2 does not vary much in the $\Delta\eta$ gap selection. However, v_2 increases with increasing $\Delta\eta$ gap in contrast to other models. This is mostly due to the fact that the TPC-FMDC correlations are influenced by jet contamination in smaller $\Delta\eta$ gap selections, as seen in the bottom panel of AMPT. In the low-p_{T} regions, v_2 values are increased by 50% and in high-p_{T} regions by a factor of 2, respectively. Since the largest $\Delta\eta$ gap has the smallest contribution from nonflow, in later sections, only results from the AMPT string melting with the gap-D are shown.

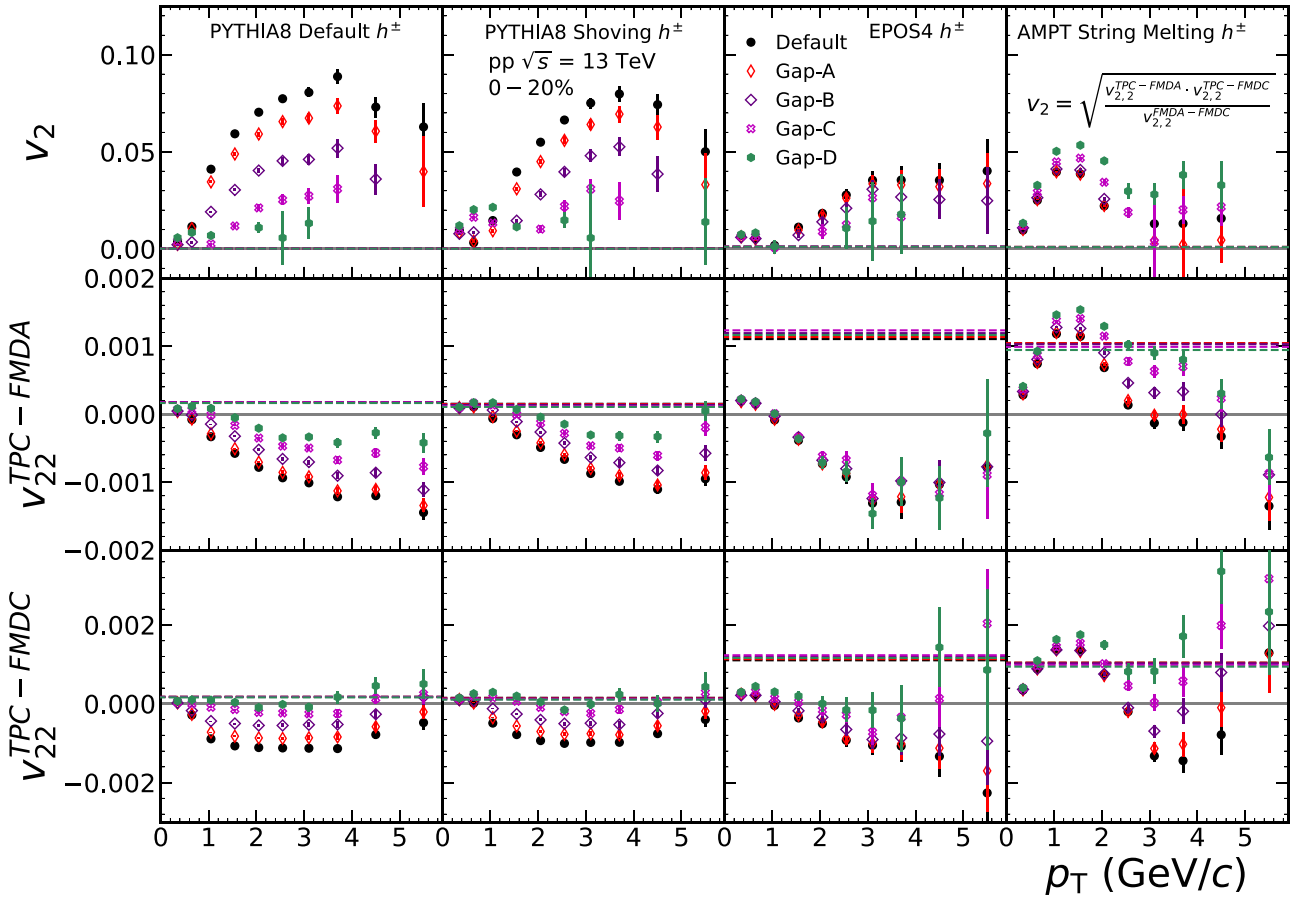

FIG. 8. The p_T-differentials v_2 for different $\Delta\eta$ gap intervals at $\sqrt{s} = 13$ TeV for several model calculations are shown for the charged particles. Two components to calculate the final v_2 on the top are shown in the bottom two rows of panels. The results of $v_{2,2}^{\mathrm{FMDA-FMDC}}$ and $v_2^{\mathrm{FMDA-FMDC}}$ are shown as dashed lines in each panel.

B. Identified charged-hadron flow

Figure 9 shows the v_2 values of the identified charged particles in 0–20% and 20–40% events with the AMPT string melting model. Grouping of v_2 is seen depending on the particle species, especially whether the particle is meson or baryon in 0–20% events. In the case of the 20–40% events,

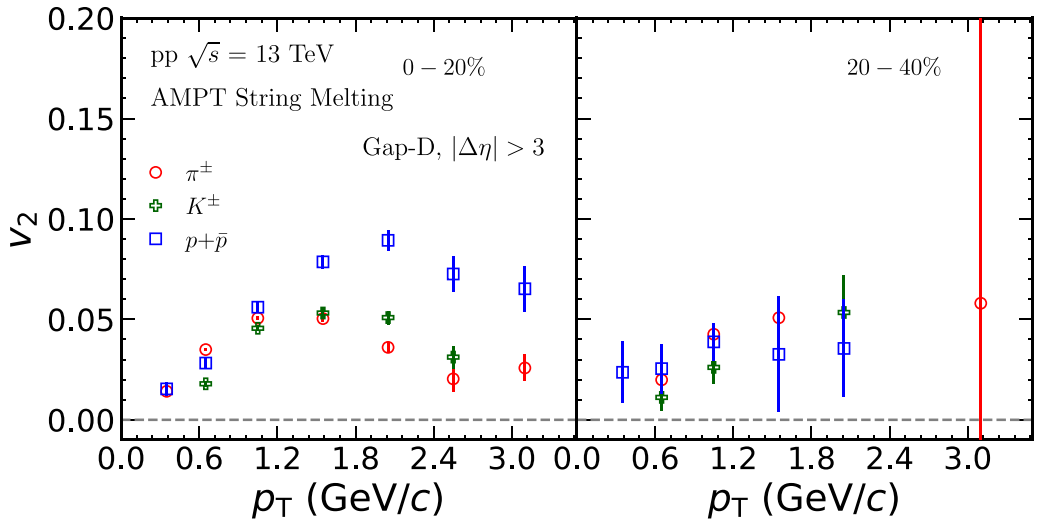

FIG. 9. The p_T-differentials v_2 for different particle species in 0–20% and 20–40% multiplicity percentiles in pp collisions at $\sqrt{s} = 13$ TeV from the AMPT string melting model calculations.

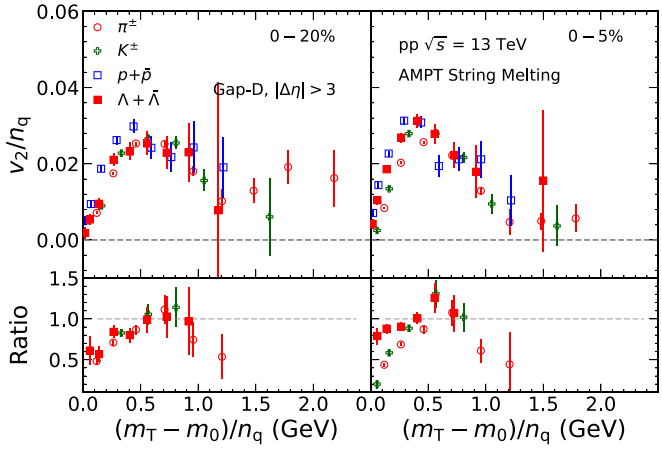

FIG. 10. The NCQ scaled m_T-dependent v_2 for different particle species in 0–20% (left) and 0–5% (right) high-multiplicity percentiles in pp collisions at $\sqrt{s} = 13$ TeV from the AMPT string melting model calculations. The ratios to proton results are shown in the bottom panels.

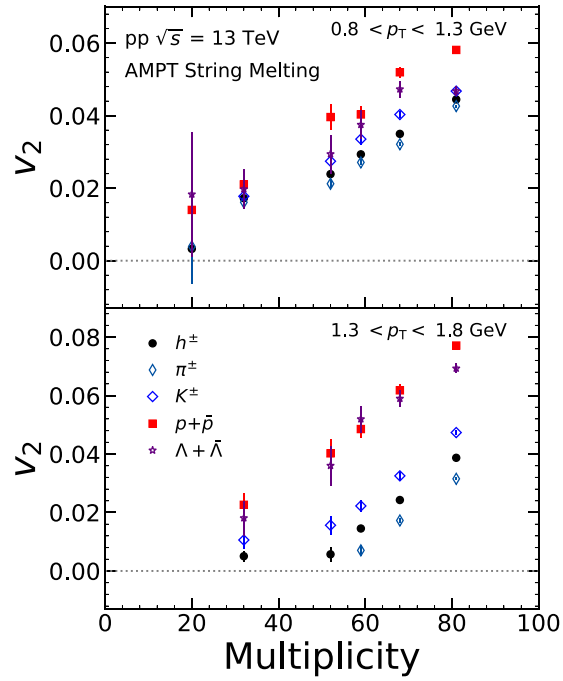

FIG. 11. The multiplicity dependence of v_2 for different particle species in pp collisions at $\sqrt{s} = 13$ TeV from the AMPT string melting model calculations.

the mass splitting is not clearly seen mostly due to the lack of statistics. Also, as smaller v_2 values are seen in 20–40% events compared to those in 0–20% events, we also studied about the multiplicity dependence of v_2.

Figure 10 shows the dependence of v_2 on transverse kinetic energy, normalized by the number of quark constituents (n_q), using the AMPT string melting model. In the model, the flow of the identified particle is a result of partonic interactions. This leads to mass ordering in the low-p_T region of the hadrons and baryon/meson grouping in the intermediate-p_T region. The results are also presented as a function of transverse kinetic energy, KE_T. This quantity is defined as $KE_T = m_T - m_0$, where $m_T = \sqrt{m_0^2 + p_T^2}$ is the transverse mass. v_2 and KE_T are then normalized by n_q, as the number of quarks in a particle varies by its type. While previous data from large collision systems at LHC show that the flow coefficients approximately lie on a line regardless of the particle species [6,34–36], the AMPT results in pp collisions show some deviation from the scaling in both 0–20% (left panels) and 0–5% (right panels) events. The ratios on the proton results in pp collisions from the AMPT calculations are very different from what is seen in the large system collisions in both the experimental data and AMPT calculations (see the Supplemental Material [73]). Experimental results obtained with the LMTF method over a wider range of p_T will provide further insight into the presence of NCQ scaling in small system collisions.

C. Multiplicity-dependent flow

In Fig. 11, we present the magnitude of v_2 as a function of multiplicity for various particle species in two p_T ranges. The $|\Delta\eta|$ range considered is > 3, and v_2 values are shown for $0.8 < p_T < 1.3$ GeV/c and $1.3 < p_T < 1.8$ GeV/c. First, we observe that the magnitude of v_2 increases with increasing multiplicity for both p_T ranges, regardless of the particle type. Second, v_2 decreases towards lower multiplicities and starts to saturate at a multiplicity of around 50. While the AMPT string melting model shows a linear multiplicity dependence, the experimental results reported in Refs. [16,17,23] show a mild decrease towards low-multiplicity events.

In the case of the higher-p_T range shown in the bottom panel of Fig. 11, we observe that the multiplicity dependence of charged hadrons differs from that of identified mesons in the first two multiplicity bins. Interestingly, baryons do not show this saturation yet in those multiplicity ranges, within the uncertainties. Furthermore, the ordering in the v_2 magnitudes between different particle species is visible, as discussed in the previous section. For both p_T ranges, the magnitudes of v_2 are clearly separated between mesons and baryons in higher multiplicities.

V. CONCLUSIONS

We extracted flow coefficients for various particle species, including π, K, p, and Λ, with identified hadrons using a few MC generators and detector combinations in wide $\Delta\eta$ ranges for pp collisions at $\sqrt{s} = 13$ TeV. The flow measurements were obtained through long-range correlations in different high-multiplicity classes by employing the LMTF method. This approach enabled us to eliminate the enhanced away-side jet fragments in high-multiplicity events relative to low-multiplicity events. However, we found that subtracting nonflow contamination in small systems could lead to biased results, due to the kinematic bias on jets and different model implementations of flow and jet components. Specifically, we observed that the PYTHIA8 default model, which does not account for collective flow, produces biased results towards large flow. Moreover, it was not possible to extract flow signals from

the EPOS4 and PYTHIA8 shoving models, which contain flow components, as they violate the assumptions of the LMTF method, containing near-side yield in low-multiplicity events. We conducted studies with the LMTF method in multiple $\Delta\eta$ gaps and found that the current ALICE η acceptance might still be influenced by nonflow contamination, suggesting the need for larger $\Delta\eta$ gaps in future analyses. Only the AMPT string melting model among the studied models was free from this bias and showed a mass ordering at low p_{T} and particle type grouping in the intermediate-p_{T} range, similar to what is observed in large systems. However, this ordering was quite distinct from that seen in large systems.

ACKNOWLEDGMENTS

We thank Klaus Werner, Christian Bierlich, and Zi-Wei Lin for fruitful discussions with their model calculations. We acknowledge CSC – IT Center for Science in Espoo, Finland, for the allocation of the computational resources. M.V., T.K., and D.J.K. are supported by the Academy of Finland, the Centre of Excellence in Quark Matter (Project No. 346328). S.J. and S.H.L. are supported by a National Research Foundation of Korea (NRF) grant funded by the Korea government (MSIT) under Contract No. 2020R1C1C1004985. We also acknowledge technical support from KIAF administrators at KISTI.

[1] J. Adams *et al.* (STAR Collaboration), Nucl. Phys. A **757**, 102 (2005).
[2] K. Adcox *et al.* (PHENIX Collaboration), Nucl. Phys. A **757**, 184 (2005).
[3] I. Arsene *et al.* (BRAHMS Collaboration), Nucl. Phys. A **757**, 1 (2005).
[4] B. B. Back *et al.* (PHOBOS Collaboration), Nucl. Phys. A **757**, 28 (2005).
[5] B. Abelev *et al.* (ALICE Collaboration), Phys. Lett. B **719**, 18 (2013).
[6] B. B. Abelev *et al.* (ALICE Collaboration), J. High Energy Phys. 06 (2015) 190.
[7] G. Aad *et al.* (ATLAS Collaboration), Phys. Lett. B **707**, 330 (2012).
[8] P. K. Kovtun, D. T. Son, and A. O. Starinets, Phys. Rev. Lett. **94**, 111601 (2005).
[9] J. E. Bernhard, J. S. Moreland, and S. A. Bass, Nat. Phys. **15**, 1113 (2019).
[10] J. Auvinen, K. J. Eskola, P. Huovinen, H. Niemi, R. Paatelainen, and P. Petreczky, Phys. Rev. C **102**, 044911 (2020).
[11] G. Nijs, W. van der Schee, U. Gürsoy, and R. Snellings, Phys. Rev. Lett. **126**, 202301 (2021).
[12] G. Nijs, W. van der Schee, U. Gürsoy, and R. Snellings, Phys. Rev. C **103**, 054909 (2021).
[13] D. Everett *et al.* (JETSCAPE Collaboration), Phys. Rev. C **103**, 054904 (2021).
[14] J. E. Parkkila, A. Onnerstad, and D. J. Kim, Phys. Rev. C **104**, 054904 (2021).
[15] J. E. Parkkila, A. Onnerstad, S. F. Taghavi, C. Mordasini, A. Bilandzic, M. Virta, and D. J. Kim, Phys. Lett. B **835**, 137485 (2022).
[16] G. Aad *et al.* (ATLAS Collaboration), Phys. Rev. Lett. **116**, 172301 (2016).
[17] V. Khachatryan *et al.* (CMS Collaboration), Phys. Rev. Lett. **116**, 172302 (2016).
[18] V. Khachatryan *et al.* (CMS Collaboration), Phys. Lett. B **765**, 193 (2017).
[19] S. Acharya *et al.* (ALICE Collaboration), Phys. Rev. Lett. **123**, 142301 (2019).
[20] M. Aaboud *et al.* (ATLAS Collaboration), Phys. Rev. C **97**, 024904 (2018).
[21] B. Abelev *et al.* (ALICE Collaboration), Phys. Lett. B **719**, 29 (2013).
[22] G. Aad *et al.* (ATLAS Collaboration), Phys. Rev. C **90**, 044906 (2014).
[23] M. Aaboud *et al.* (ATLAS Collaboration), Phys. Rev. C **96**, 024908 (2017).
[24] V. Khachatryan *et al.* (CMS Collaboration), Phys. Rev. C **96**, 014915 (2017).
[25] C. Aidala *et al.* (PHENIX Collaboration), Nat. Phys. **15**, 214 (2019).
[26] C. Aidala *et al.* (PHENIX Collaboration), Phys. Rev. Lett. **120**, 062302 (2018).
[27] A. Bilandzic, R. Snellings, and S. Voloshin, Phys. Rev. C **83**, 044913 (2011).
[28] M. Aaboud *et al.* (ATLAS Collaboration), Phys. Lett. B **789**, 444 (2019).
[29] S. Chatrchyan *et al.* (CMS Collaboration), Eur. Phys. J. C **73**, 2674 (2013).
[30] J. Adams *et al.* (STAR Collaboration), Phys. Rev. Lett. **92**, 052302 (2004).
[31] B. I. Abelev *et al.* (STAR Collaboration), Phys. Rev. C **75**, 054906 (2007).
[32] S. S. Adler *et al.* (PHENIX Collaboration), Phys. Rev. Lett. **91**, 182301 (2003).
[33] A. Adare *et al.* (PHENIX Collaboration), Phys. Rev. Lett. **98**, 162301 (2007).
[34] J. Adam *et al.* (ALICE Collaboration), Phys. Rev. C **93**, 034916 (2016).
[35] J. Adam *et al.* (ALICE Collaboration), J. High Energy Phys. 09 (2016) 164.
[36] S. Acharya *et al.* (ALICE Collaboration), J. High Energy Phys. 09 (2018) 006.
[37] S. Acharya *et al.* (ALICE Collaboration), J. High Energy Phys. 05 (2023) 243.
[38] L. Zheng, H. Li, H. Qin, Q.-Y. Shou, and Z.-B. Yin, Eur. Phys. J. A 05 (2017) 124.
[39] J. C. Dunlop, M. A. Lisa, and P. Sorensen, Phys. Rev. C **84**, 044914 (2011).
[40] S. Singha and M. Nasim, Phys. Rev. C **93**, 034908 (2016).
[41] V. Pacík (ALICE Collaboration), Nucl. Phys. A **982**, 451 (2019).
[42] A. Adare *et al.* (PHENIX Collaboration), Phys. Rev. C **97**, 064904 (2018).
[43] B. Schenke, C. Shen, and P. Tribedy, Phys. Rev. C **102**, 044905 (2020).
[44] M. Strickland, Nucl. Phys. A **982**, 92 (2019).
[45] C. Loizides, Nucl. Phys. A **956**, 200 (2016).
[46] J. L. Nagle and W. A. Zajc, Annu. Rev. Nucl. Part. Sci. **68**, 211 (2018).

[47] M. Gyulassy and M. Plumer, Phys. Lett. B **243**, 432 (1990).
[48] X.-N. Wang and M. Gyulassy, Phys. Rev. Lett. **68**, 1480 (1992).
[49] J. Adam *et al.* (ALICE Collaboration), Phys. Rev. C **91**, 064905 (2015).
[50] V. Khachatryan *et al.* (CMS Collaboration), J. High Energy Phys. 04 (2017) 039.
[51] J. Adam *et al.* (ALICE Collaboration), Eur. Phys. J. C **76**, 271 (2016).
[52] J. Adam *et al.* (ALICE Collaboration), Phys. Lett. B **760**, 720 (2016).
[53] S. Acharya *et al.* (ALICE Collaboration), Phys. Lett. B **783**, 95 (2018).
[54] J. Adam *et al.* (ALICE Collaboration), Phys. Rev. Lett. **119**, 102301 (2017).
[55] Z.-W. Lin, C. M. Ko, B.-A. Li, B. Zhang, and S. Pal, Phys. Rev. C **72**, 064901 (2005).
[56] C. Bierlich, G. Gustafson, and L. Lönnblad, Phys. Lett. B **779**, 58 (2018).
[57] C. Bierlich, Phys. Lett. B **795**, 194 (2019).
[58] T. Pierog, I. Karpenko, J. M. Katzy, E. Yatsenko, and K. Werner, Phys. Rev. C **92**, 034906 (2015).
[59] P. Skands, S. Carrazza, and J. Rojo, Eur. Phys. J. C **74**, 3024 (2014).
[60] S. H. Lim, Q. Hu, R. Belmont, K. K. Hill, J. L. Nagle, and D. V. Perepelitsa, Phys. Rev. C **100**, 024908 (2019).
[61] S. Acharya *et al.* (ALICE Collaboration), J. High Energy Phys. 05 (2021) 290.
[62] J. Kim, E.-J. Kim, S. Ji, and S. Lim, J. Korean Phys. Soc. **79**, 447 (2021).
[63] J. D. Orjuela Koop, A. Adare, D. McGlinchey, and J. L. Nagle, Phys. Rev. C **92**, 054903 (2015).
[64] K. Gallmeister, H. Niemi, C. Greiner, and D. H. Rischke, Phys. Rev. C **98**, 024912 (2018).
[65] A. Kurkela, U. A. Wiedemann, and B. Wu, Eur. Phys. J. C **79**, 965 (2019).
[66] A. Kurkela, S. F. Taghavi, U. A. Wiedemann, and B. Wu, Phys. Lett. B **811**, 135901 (2020).
[67] V. E. Ambrus, S. Schlichting, and C. Werthmann, Phys. Rev. D **105**, 014031 (2022).
[68] K. Werner, B. Guiot, I. Karpenko, and T. Pierog, Phys. Rev. C **89**, 064903 (2014).
[69] S. Acharya *et al.* (ALICE Collaboration), Eur. Phys. J. C **81**, 630 (2021).
[70] K. Aamodt *et al.* (ALICE Collaboration), J. Instrum. **3**, S08002 (2008).
[71] E. Abbas *et al.* (ALICE Collaboration), J. Instrum. **8**, P10016 (2013).
[72] G. Aad *et al.* (ATLAS Collaboration), Phys. Rev. Lett. **110**, 182302 (2013).
[73] See Supplemental Material at http://link.aps.org/supplemental/10.1103/PhysRevC.108.034909 for LMTF method and two-particle correlation functions used in the paper in further detail with additional results from AMPT model calculations and it includes Refs. [74,75].
[74] N. Mallick, S. Prasad, A. N. Mishra, R. Sahoo, and G. G. Barnaföldi, Phys. Rev. D **107**, 094001 (2023).
[75] J. Adams *et al.* (STAR Collaboration), Phys. Rev. C **72**, 014904 (2005).